UWB-aided GNSS/INS fusion for resilient positioning in GNSS challenged environments

Christophe Villien, Benoit Denis

UWB-aided GNSS/INS Fusion for Resilient Positioning in GNSS Challenged Environments

Christophe Villien, Benoît Denis
CEA-Leti
Université Grenoble Alpes
F-38000 Grenoble, France
(christophe.villien, benoit.denis)@cea.fr

***Abstract*—The fusion of Inertial Navigation System (INS) and Global Navigation Satellite System (GNSS) is a well established technique to provide resilient positioning even in GNSS challenged environments. However, when GNSS reception conditions are persistently degraded, the inherent drift of inertial navigation can result in insufficient accuracy (e.g. greater than 1m), especially when using industrial or tactical grade Inertial Measurement Unit (IMU). This study introduces the tightly coupled integration of Ultra-Wideband (UWB) ranging measurements with fixed beacons to a loosely coupled GNSS/INS fusion. The algorithm uses an Error-State Kalman Filter (ES-KF) that supports Velocity Constraints (VC) and Zero-Angular Rate Updates (ZARU)/Zero Velocity Updates (ZVU). It details the necessary pre-processing of UWB measurements to correct for clock drift, velocity and latency errors, and provides two calibration techniques suitable for guided and generic use cases, resulting in ranging accuracy of better than 3cm and 11cm, respectively, based on 28 field tests. The benefits of UWB measurements in fusion are demonstrated through a field trial with severely degraded GNSS conditions, resulting in horizontal accuracy better than 40cm (compared to 2.1m without UWB) and improved rejection of poor GNSS measurements.**

***Index Terms*—Inertial Navigation System (INS),Global Navigation Satellite System (GNSS), Ultra-Wideband (UWB), GNSS/INS/UWB fusion, Error-State Kalman Filter (ES-KF), UWB calibration**

I. Introduction

Although Global Navigation Satellite System (GNSS) is a quite old and well-established technology, it has been constantly improved for the last past decade, with the dramatic increase of the number of available signals (e.g., Galileo) or with the introduction of high performance receivers at reasonable costs (e.g., consumer grade dual-band RTK receiver), which can provide sub-meter accuracy even in standalone mode. If such performance levels can generally fulfil the requirements of many outdoor applications in a variety of domains (e.g., standard vehicles navigation, logistics and works, sports, etc.), the fusion with an Inertial Navigation System (INS) is generally preferred whenever the positioning quality is critical (e.g., military or safety applications, autonomous driving, etc.) and service availability must be guaranteed regardless of the operating conditions (e.g., incl. in GNSS challenged environments, such as urban canyons or tunnels). However, if the system must integrate an industrial or tactical grade Inertial Measurement Unit (IMU) under costs restriction constraints (rather than a navigation grade IMU of several tens of thousands of US dollars), it is then difficult to maintain the required meter-scale accuracy when GNSS outages are not transient but may last for a few minutes, due to well-known INS position drift effects [1]. This situation can occur rather frequently in concrete applications like construction sites monitoring, where it is necessary to track construction equipment or vulnerable workers for security reasons. GNSS signals can indeed be durably degraded in such working contexts, as some agents may stay in GNSS-denied zones for long periods of time, especially when the worksite is located in dense urban environments or on rough natural terrains (e.g., in mountain areas, close to vertical cliffs, etc.). In such a case, the use of complementary local radio signals like that of Ultra-Wideband (UWB) beacons seem particularly well-suited [2]. The latter offer sub-meter accuracy at reasonable costs (e.g., typ. less than 100 US dollars and even down to a few US dollars, depending on the standard and level of hardware integration), provide coverage up to a hundred of meters and can be deployed in an opportunistic manner. Thanks to their large bandwidth (i.e. >500MHz typ.), Impulse Radio - UWB (IR-UWB) waveforms indeed allow to measure the Time of Arrival (TOA) of transmitted signals within sub-nanosecond accuracy, which translates into a ranging precision of a few tenth of centimeters when a multi-way ranging (TWR) scheme is used for instance [3]. In addition, in a context of GNSS/INS data fusion, a full coverage of say, 3 UWB beacons (i.e., typ. required to solve a 2D positioning problem from range measurements through trilateration), is not mandatory because measurements from a single or two beacons can already be beneficial and help to contain the position drift. Recently, authors in [4]–[6] have hence considered deploying such UWB beacons in GNSS-challenged environments. While fusion is generally based on an Error State - Kalman Filter (ES-KF), where the state vector represents corrections of the INS solution [4]–[7], several architectures have been considered in this context, which differentiate from each others in the nature of the measurements used to correct the solution. In [4], two independent GNSS and UWB positions are computed in a first step, and compared to update the INS solutions. This architecture, which can be referred to as GNSS-loosely coupled and UWB-loosely coupled, requires a minimum of

4 valid satellites or a minimum of 3 UWB beacons (in the TWR scheme). Given typical UWB transmission ranges (in practice, on the order of a few 100s of meters at most), this approach requires a dense terrestrial infrastructure to ensure good coverage and accordingly, service continuity. Other authors have studied UWB-tightly coupled and GNSS-loosely coupled [8] and both UWB and GNSS tightly coupled [5] solutions, which could benefit from a single UWB link (i.e., with respect to one beacon) to correct the solution, even if the presented results are still based in practice on several in-coverage beacons. Moreover, the preliminary validation and/or early pre-processing of the raw measurements to be used in the solution update (i.e., GNSS signals/position/velocity, UWB measurements), which may be affected by strong outliers or biases, has not been really discussed either. In particular, just like GNSS signals, UWB signals may be altered by reflections and/or obstructions, resulting in possibly large ranging errors. The latter should hence be detected by the fusion algorithm and excluded from the solution update. In addition, since the UWB ranging acquisition process is not instantaneous but can last for up to a few hundred of milliseconds within typical protocol settings, it is notorious that mobility introduces extra ranging errors caused by the relative displacement of the involved radio transceivers during the ranging process [9]. This phenomenon is even more significant in a data fusion context, as the computed range is generally delayed with respect to the current INS solution. In contrast to these works, the proposed solution addresses the various issues cited above through a fusion algorithm based on an ES-KF resolved in the Earth-Centered, Earth-Fixed (ECEF) frame, with estimation of the IMU biases, as well as of odometer scale factor errors, while relying on loosely coupled GNSS measurements, tightly coupled UWB measurements, odometer measurements, velocity constraints (VC) and Zero Angular Rates / Zero Velocity Updates (ZARU / ZVU). In our experimental validations, we have deliberately focused on a highly challenging study case (i.e., a typical urban canyon under typical vehicular mobility) so as to assess the robustness of our fusion solution and concretely illustrate operating contexts where it could be truly beneficial. Besides, the pre-processing of UWB measurements has also been subject to extensive field tests, which represent in themselves another contribution of the paper.

This paper is organized as follows. In sec. II, the ES-KF algorithm designed for data fusion will be presented. Then, in sec. III, a detailed description of the UWB measurements (incl. various calibration procedures) will be provided. Finally, the performance of both UWB pre-processing and fused positioning steps will be evaluated in sec. IV based on field tests.

II. Integrated Multi-Sensor Navigation Model

The architecture of the developed integrated multi-sensor navigation system is illustrated in Fig. 1. The INS block delivers a full solution comprising attitude, position and velocity (APV) computed from the IMU readings, which are corrected, as well as the sensors biases, by an ES-KF [10], resulting in a closed-loop architecture. The latter uses position and velocity outputs from the GNSS receiver, which corresponds to a loosely-coupled integration, but also range measurements directly from the UWB block, corresponding to a tightly-coupled integration. The "static detector" block is used to detect static phases and triggers the ZVU and ZARU [10]. Not represented on the figure for the sake of diagram readability, the ES-KF also applies velocity constraints [10] to the solution for relevant applications (e.g. road vehicles, trains, etc.), where the motion is constrained. The UWB block controls radio exchanges, computes raw ranges from the TOA measurements, and applies compensations and calibration to these raw ranges to correct specific errors, as described in sec. III. One of the main advantage of this architecture based on an ES-KF in comparison with a standard total-state Kalman Filter (i.e., which tracks the full system instead of the corrections only), is that state propagation is executed at the GNSS or UWB rate (e.g. 10Hz) instead of the INS rate (e.g. 200Hz), thus reducing the computational burden.

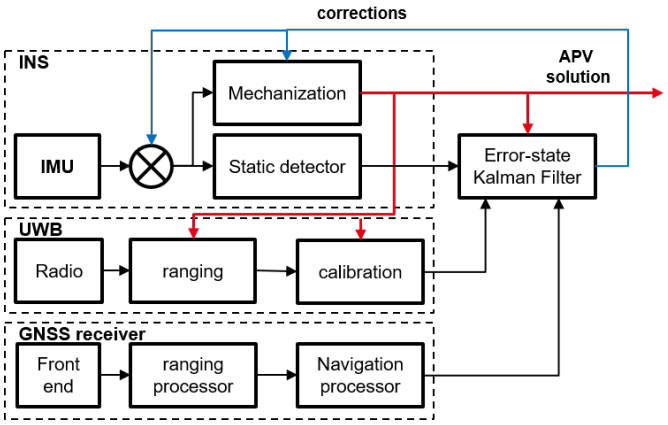

Fig. 1. Proposed fusion architecture.

A. Inertial navigation

Inertial navigation corresponds to the integration of the IMU measurements by the mechanization block (see Fig. 1) to update the APV solution which is, in our case, resolved in the ECEF coordinate system. The raw inertial solution is computed using standard equations from [10, pp. 175-188] and comprises $\tilde{\mathbf{C}}_b^e$, the rotation matrix from the body frame to the ECEF frame, as well as $\tilde{\mathbf{r}}_{eb}^e$ and $\tilde{\mathbf{v}}_{eb}^e \in \mathbb{R}^3$, the position and velocity vectors resolved in ECEF frame.

B. State model

In an ES-KF architecture, the estimated state $\hat{\mathbf{x}}_k \in \mathbb{R}^{15}$ comprises the errors of the system:

$$\hat{\mathbf{x}}_k = \begin{bmatrix} \delta\hat{\boldsymbol{\Psi}}_{eb}^e & \delta\hat{\mathbf{v}}_{eb}^e & \delta\hat{\mathbf{r}}_{eb}^e & \delta\hat{\mathbf{b}}_a & \delta\hat{\mathbf{b}}_g \end{bmatrix}^T \quad (1)$$

where $\delta\hat{\boldsymbol{\Psi}}_{eb}^e$, $\delta\hat{\mathbf{v}}_{eb}^e$ and $\delta\hat{\mathbf{r}}_{eb}^e$ represent the vectors ($\in \mathbb{R}^3$) of angular, velocity and position errors and $\delta\hat{\mathbf{b}}_a$ and $\delta\hat{\mathbf{b}}_g$ the vectors ($\in \mathbb{R}^3$) of accelerometer and gyroscope biases errors

respectively [10]. The corrected system state is the given by [10, p. 563]

$$\hat{\mathbf{C}}_b^e = \left(\mathbf{I}_3 - [\delta\hat{\mathbf{\Psi}}_{eb}^e\wedge]\right)\tilde{\mathbf{C}}_b^e \tag{2}$$
$$\hat{\mathbf{v}}_{eb}^e = \tilde{\mathbf{v}}_{eb}^e - \delta\hat{\mathbf{v}}_{eb}^e \tag{3}$$
$$\hat{\mathbf{r}}_{eb}^e = \tilde{\mathbf{r}}_{eb}^e - \delta\hat{\mathbf{r}}_{eb}^e \tag{4}$$
$$\hat{\mathbf{b}}_a = \tilde{\mathbf{b}}_a + \delta\hat{\mathbf{b}}_a \tag{5}$$
$$\hat{\mathbf{b}}_g = \tilde{\mathbf{b}}_g + \delta\hat{\mathbf{b}}_g \tag{6}$$

with $\mathbf{I}_3$ the 3×3 identity matrix and $[a\wedge]$ the skew symmetric matrix constructed from vector a (see [10, p. 45]).

C. State and covariance propagation

According to the error-state architecture, the state and its covariance matrix $\mathbf{P}_k$ are propagated from time t_k to time t_{k+1} using the well known equations

$$\hat{\mathbf{x}}_k^- = \mathbf{\Phi}_{k-1}\hat{\mathbf{x}}_{k-1}^+ \tag{7}$$
$$\mathbf{P}_k^- = \mathbf{\Phi}_{k-1}\mathbf{P}_{k-1}^+{\mathbf{\Phi}_{k-1}}^T + \mathbf{Q}_{k-1} \tag{8}$$

Because in the chosen architecture the estimated errors $\hat{\mathbf{x}}_k$ of the system are continuously integrated, the initial state is always null $\hat{\mathbf{x}}_{k-1}^+ = \mathbf{0}_{15}$, and the state propagation step can hence be skipped. The propagation of the covariance matrix can be computed using the transition matrix $\mathbf{\Phi}_{k-1}$ in [10, p. 584] and the covariance matrix matrix of the state noise $\mathbf{Q}_{k-1}$ in [10, p. 592].

D. State and covariance updates

The predicted state $\hat{\mathbf{x}}_k^-$ and covariance $\mathbf{P}_k^-$ are then updated from the measurements $\delta\mathbf{z}_k$ through the following steps

$$\mathbf{C}_k = \mathbf{H}_k\mathbf{P}_k^-{\mathbf{H}_k}^T + \mathbf{R}_k \tag{9}$$
$$\mathbf{K}_k = \mathbf{P}_k^-{\mathbf{H}_k}^T\mathbf{C}_k \tag{10}$$
$$\mathbf{x}_k^+ = \mathbf{K}_k\delta\mathbf{z}_k \tag{11}$$
$$\mathbf{P}_k^+ = \left(\mathbf{I}_{15} - \mathbf{K}_k\mathbf{H}_k\right)\mathbf{P}_k^- \tag{12}$$

with $\delta\mathbf{z}_k$ the innovation, $\mathbf{C}_k$ the covariance of innovation, $\mathbf{K}_k$ the Kalman gain, $\mathbf{H}_k$ the observation matrix and $\mathbf{R}_k$ the covariance of measurement noise. Note that in the ES-KF the measurements are equal to the innovation as the predicted error (i.e. $\mathbf{H}_k\hat{\mathbf{x}}_k^-$) is always null. Because all the measurements (i.e., possibly up to $11+n$ measurements in our case, with n the number of UWB measurements) are not available or valid for every update, they are selected as well as their associated covariance and observation matrix using a selection matrix $\mathbf{S}_k$

$$\delta\mathbf{z}_k = \mathbf{S}_k\mathbf{z}_k^* \quad \mathbf{R}_k = \mathbf{S}_k\mathbf{R}_k^*{\mathbf{S}_k}^T \quad \mathbf{H}_k = \mathbf{S}_k\mathbf{H}_k^* \tag{13}$$

with $\mathbf{z}_k^*$, $\mathbf{R}_k^*$ and $\mathbf{H}_k^*$ the concatenation of all possible measurements, noise covariance and observation sub-matrices before the selection, as follows

$$\delta\mathbf{z}_k^* = \begin{bmatrix}\delta\mathbf{z}_{pos,k}^T & \delta\mathbf{z}_{vel,k}^T & \delta\mathbf{z}_{VC,k}^T & \delta\mathbf{z}_{ZARU,k}^T & \delta\mathbf{z}_{UWB,k}^T\end{bmatrix}^T \tag{14}$$

$$\mathbf{R}_k^* = \begin{bmatrix}\mathbf{R}_{pos,k} & \mathbf{0}_{3\times3} & \mathbf{0}_{3\times2} & \mathbf{0}_{3\times3} & \mathbf{0}_{3\times n}\\ \mathbf{0}_{3\times3} & \mathbf{R}_{vel,k} & \mathbf{0}_{3\times2} & \mathbf{0}_{3\times3} & \mathbf{0}_{3\times n}\\ \mathbf{0}_{2\times3} & \mathbf{0}_{2\times3} & \mathbf{R}_{VC,k} & \mathbf{0}_{2\times3} & \mathbf{0}_{2\times n}\\ \mathbf{0}_{3\times3} & \mathbf{0}_{3\times3} & \mathbf{0}_{3\times2} & \mathbf{R}_{Z,k} & \mathbf{0}_{3\times n}\\ \mathbf{0}_{n\times3} & \mathbf{0}_{n\times3} & \mathbf{0}_{n\times2} & \mathbf{0}_{n\times3} & \mathbf{R}_{UWB,k}\end{bmatrix} \tag{15}$$

$$\mathbf{H}_k^* = \begin{bmatrix}\mathbf{H}_{pos,k}^T & \mathbf{H}_{vel,k}^T & \mathbf{H}_{VC,k}^T & \mathbf{H}_{Z,k}^T & \mathbf{H}_{UWB,k}^T\end{bmatrix}^T \tag{16}$$

The selection matrix $\mathbf{S}_k$ is build as an identity matrix $\mathbf{I}_{11+n}$ where the lines of the missing measurements are removed. As an example, assuming that only GNSS position and velocity are valid for update, the selection matrix would be

$$\mathbf{S}_k = \mathbf{S}_k^{pos,vel} = \begin{bmatrix}\mathbf{I}_3 & \mathbf{0}_{3\times3} & \mathbf{0}_{3\times2} & \mathbf{0}_{3\times3} & \mathbf{0}_{3\times n}\\ \mathbf{0}_{3\times3} & \mathbf{I}_3 & \mathbf{0}_{3\times2} & \mathbf{0}_{3\times3} & \mathbf{0}_{3\times n}\end{bmatrix} \tag{17}$$

A detailed description of the related formulas can be found in [10]

- GNSS position ($\delta\mathbf{z}_{pos,k}$, $\mathbf{H}_{pos,k}$, $\mathbf{R}_{pos,k}$) [p. 598, 600]
- GNSS velocity ($\delta\mathbf{z}_{vel,k}$, $\mathbf{H}_{vel,k}$, $\mathbf{R}_{vel,k}$) [p. 598, 600]
- VC ($\delta\mathbf{z}_{VC,k}$, $\mathbf{H}_{VC,k}$, $\mathbf{R}_{VC,k}$) [pp. 641-642]
- ZARU ($\delta\mathbf{z}_{ZARU,k}$, $\mathbf{H}_{ZARU,k}$, $\mathbf{R}_{ZARU,k}$) [pp. 641-642]

E. UWB measurement integration

For improved readability, the UWB antenna of the mobile transceiver will hereafter be referred to simply as the *UWB antenna* and the UWB antenna of the fixed beacon will be referred to as the *UWB beacon*. The UWB measurement $\delta\mathbf{z}_{UWB_i,k}$ from beacon #*i* with coordinates $\mathbf{r}_i$ is given by

$$\delta\mathbf{z}_{UWB_i,k} = d_i - \left\|\hat{\mathbf{r}}_{eb}^e + \hat{\mathbf{C}}_b^e\mathbf{l}_{bu}^b - \mathbf{r}_i\right\| \tag{18}$$

with d_i the distance between UWB antenna and the UWB beacon, $\mathbf{l}_{bu}^b \in \mathbb{R}^3$ the lever arm between the origin of the body frame and the UWB antenna. The observation matrix is, by definition

$$\mathbf{H}_{UWB_i,k} = \begin{bmatrix}\frac{\partial\delta\mathbf{z}_{UWB_i,k}}{\partial\delta\hat{\mathbf{\Psi}}_{eb}^e} & \mathbf{0}_{1\times3} & \frac{\delta\mathbf{z}_{UWB_i,k}}{\partial\delta\hat{\mathbf{r}}_{eb}^e} & \mathbf{0}_{1\times3} & \mathbf{0}_{1\times3}\end{bmatrix} \tag{19}$$

Neglecting the effect of attitude error on the innovation through the lever arm, the observation matrix is simply

$$\mathbf{H}_{UWB_i,k} = \begin{bmatrix}\mathbf{0}_{1\times3} & \mathbf{0}_{1\times3} & \mathbf{u}_i^{eT} & \mathbf{0}_{1\times3} & \mathbf{0}_{1\times3}\end{bmatrix} \tag{20}$$

with the unit vector $\mathbf{u}_i^e$ from the UWB antenna to the UWB beacon

$$\mathbf{u}_i^e = \frac{\mathbf{r}_i - \hat{\mathbf{r}}_{eb}^e}{\|\mathbf{r}_i - \hat{\mathbf{r}}_{eb}^e\|} \tag{21}$$

The UWB measurements are assumed to be independent and their noise is assumed to follow a centered Gaussian distribution with standard deviation $\sigma_{UWB,i}$, and thus, the covariance matrix of measurement noise is diagonal with the element i,i equal to

$$\left[\mathbf{R}_{UWB,k}\right]_{i,i} = \sigma_{UWB,i}^2 \tag{22}$$

F. Measurement selection

Not all the measurements are used for each update as some could be unavailable (e.g. during a GNSS or UWB outage) or because they might be detected as invalid in the presence of outliers for instance. The selection matrix is used to manage the measurements that are actually used for the state update, as described in ((13)). The ZARU and ZVU measurements (i.e. $\delta \mathbf{z}_{ZARU,k}$) are used whenever a static phase is detected by the static detector depicted in Fig. 1, whose functioning falls beyond the scope of this paper. The VC measurements, which assume null velocities along the side and the vertical axis of a vehicle for instance, are always available in relevant applications, excepted when the angular velocity along the vertical axis exceeds a certain value (e.g., 0.05 rad/s), as it may cause some side slips, which invalidate the transverse velocity constraint [10, p. 642]. For the GNSS velocity, position and UWB ranges, in addition to their availability, an extra test based on innovation monitoring is performed to check their integrity. The value $[\delta \mathbf{z}_k]_i$, which also corresponds to the innovation in ES-KF, is compared to a threshold determined by the predicted covariance of the innovation

$$|\delta \mathbf{z}_i| < k\sqrt{[\mathbf{C}_k]_{i,i}} \tag{23}$$

with $[\mathbf{C}_k]_{i,i}$ the diagonal term i,i of the innovation covariance in ((9)), and k a multiplying factor that sets the tolerance for measurement selection (e.g., k=3).

III. UWB PREPROCESSING

As already mentioned, UWB technology refers to a radio waveform occupying a very-large bandwidth (i.e., typ. $>$ 500MHz) allowing very accurate (e.g., below 1 ns) TOA measurements and, accordingly, accurate ranging measurements (e.g., within 10 cm accuracy). However, if decimeter accuracie are frequently reported, more important attention should be paid to the UWB integration, especially in the context of data fusion and mobility. The well known round-trip time of flight formula that provides the raw distance d_{raw} without any compensation is given by

$$d_{raw} = \frac{c}{2}(T^A_{round} - T^B_{reply}) \tag{24}$$

with $T^A_{round} = t^A_4 - t^A_1$ and $T^B_{round} = t^B_3 - t^B_2$, which are both defined as the difference between a time of departure (TOD) and a TOA, measured by devices A and B respectively (see Fig. 2). However, this measured raw distance can be related to the true distance d through

$$d_{raw} = d + \delta d_{clk} + \delta d_{vel} + \delta d_{cal} \tag{25}$$

with δd_{clk} and δd_{vel} some ranging errors caused by the relative clock drift and velocity between devices A and B respectively, and δd_{cal} a ranging error introduced by the transceiver and, eventually, further propagation effects that can be calibrated.

A. Periodic two-way ranging with clock drift compensation

UWB ranging relies on transmissions between two devices having independent clocks whose relative offsets and drifts must be estimated. This is generally performed using Symmetrical Double Side-Two Way Ranging (SDS-TWR) [11], which requires 3 transmissions to estimate clock offset and drift. Alternatively, for periodic transmissions where a superframe is repeated with a period T_{SF}, periods T^A_{SF} and T^B_{SF} measured by clock A and B respectively (see Fig. 2) can be used to produce an estimate ϵ^B_A of the relative clock drift of clock B with respect to clock A

$$\epsilon^B_A = T^A_{SF}/T^B_{SF} - 1 \tag{26}$$

Noting that $T^A_{reply} = (\epsilon^B_A + 1)T^B_{reply}$ and applying TWR ranging formulas [11] yields the compensated measured distance d_{comp}

$$d_{comp} = \frac{c}{2}(T^A_{round} - T^B_{reply} - \epsilon^B_A T^B_{reply}) \tag{27}$$

with c the speed of light. The clock drift compensation term in this formula is

$$\delta d_{clk} = -\frac{c}{2}(\epsilon^B_A T^B_{reply}) \tag{28}$$

It is to be noticed that this formula is written for clock A, hence the error of the distance computation is of the same order of magnitude as that of the absolute clock drift of clock A, typically about a tenth of part-per-million (ppm), depending on the crystal used, but could generally be neglected. Most importantly, it assumes no variation of the clock drift between consecutive superframes, which may be violated especially during warm-up or for long T_{SF} periods.

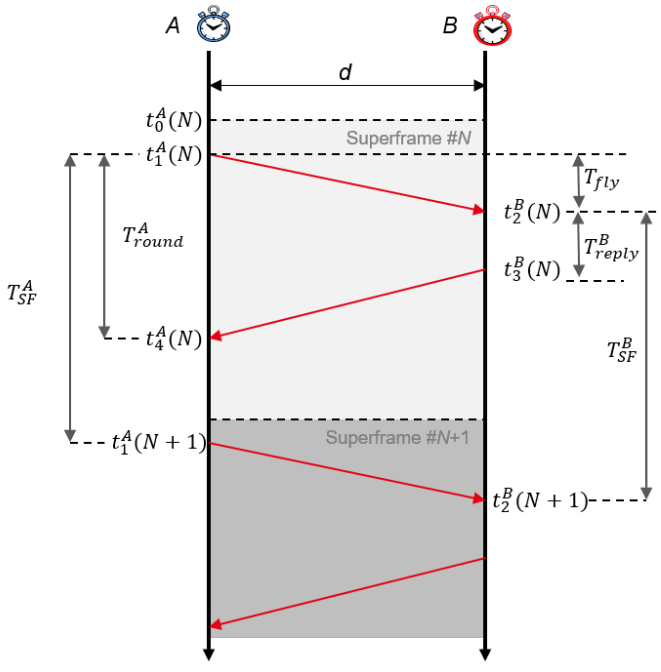

Fig. 2. Periodic two-way ranging.

B. Velocity compensation

The compensated ranging formula in (27) also assumes a constant distance during the entire ranging process, which may be not valid in case of mobility [9]. In addition, in a fusion context, one must consider the actual time at which the distance is computed to ensure space-time consistency with the other used sensors. As an example, considering typical refresh periods of 100ms for both GNSS and UWB, and a car driving at 15m/s, a lack of accurate synchronization between the time corresponding to GNSS position and the time of UWB ranging could result into an inconsistency of up to 1.5m, that is to say, much more than the expected UWB ranging accuracy. The proposed UWB ranging model computes the distance d_0 at a given reference time t_0, which we assume to be synchronized with the GNSS time using the pulse-per-second (PPS) signal delivered by the receiver for instance. We also assume a constant apparent velocity v^r_{AB} of B with respect to A during the ranging process. As illustrated in Fig. 3, the main consequence of mobility is the introduction of two extra-propagation times δt^B_{v1} and δt^B_{v2} due to the increased distance at the times of transmission. Arrival time t^B_2 can be solved easily when considering it as the solution of the problem of a "race" between receiver B, starting at e.g., $t = t^A_0 = 0$, and "running" at velocity v on the one hand, and the radio wave, transmitted by device A but starting with a delay t^A_1 in addition to an handicap d_0, and "flying" at velocity c on the hand, resulting in the following equation

$$c.(t^B_2 - t^A_1) = v.t^B_2 + d_0 \tag{29}$$

The arrival time is hence solved easily as

$$t^B_2 = \frac{d_0 + t^A_1.c}{c - v} \tag{30}$$

Extra times δt^B_{v1} and δt^B_{v1} can be obtained by subtracting the same term in (30) taking $v = 0$

$$\delta t^B_{v2} = t^B_2 - \left(\frac{d_0}{c} + t^A_1\right) \tag{31}$$

wich yields, in the general case where $t^A_0 \neq 0$

$$\delta t^B_{v2} = \frac{v}{c - v}\left(\frac{d_0}{c} + (t^A_1 - t^A_0)\right) \tag{32}$$

and

$$\delta t^B_{v3} = \frac{v}{c - v}\left((t^A_4 - t^A_0) - \frac{d_0}{c}\right) \tag{33}$$

Noting that $v \ll c$ and $d_0/c \ll (t^A_1 - t^A_0)$, the distance d_0 is given by

$$d_0 = d_{raw} - \delta d_{vel} \tag{34}$$

with the velocity correction term

$$\delta d_{vel} = \frac{v}{2}\left((t^A_1 - t^A_0) + (t^A_4 - t^A_0)\right) \tag{35}$$

which is nothing else but the average travelled distance between the beginning and the end of the ranging process. It should also be noted that, in the context of fusion, the apparent velocity can easily be computed from the INS solution $\tilde{\mathbf{v}}^e_{eb}$.

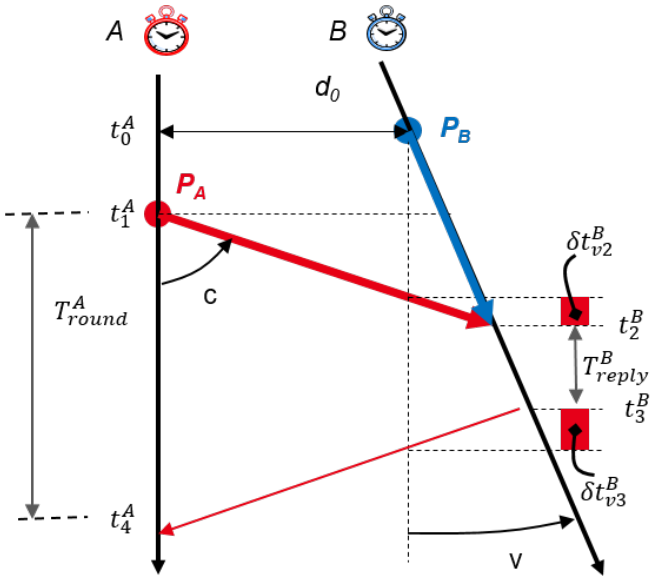

Fig. 3. Two-way ranging scheme in mobility

C. Range calibration

Although the standard deviation of the measured distances is typically about a tenth of centimeters, a much larger bias may exist, due to the transceiver itself and/or to the propagation conditions. This bias δd_{cal} could be split in a constant term ρ_{b0} and a varying term ρ_{bd}, which usually depends on the received signal strength (RSS) and/or the propagating conditions

$$\delta d_{cal} = \rho_{b0} + \rho_{bd} \tag{36}$$

For instance, the DW1000 from decawave exhibits a bias of about $\rho_{b0} \approx 154m$, and a variable component ρ_{bd} that depends on the RSS and may vary in a range of 25cm according to its manufacturer [12]. However such a compensation is not always efficient in practice as it does not really account for propagation conditions. For instance, in our tests (see sec. IV-A), the ρ_{bd} component was varying in a 80cm range. In our approach, we have adopted two different strategies depending on the use case. For guided applications (e.g., railway, subway, cable-cars, etc.), all possible positions belongs to a finite number of (e.g., 4) segments. Typically, each track is divided into 2 segments (i.e., one each side of the fixed UWB beacon, see Fig. 7) to distinguish between different propagation conditions (i.e., on one side, the radio wave propagates toward the front of the vehicle, whereas on the other side, it propagates toward the back of the vehicle). Then, a compensation table is build for each segment during a calibration phase where the true distance should be obtained using a reference system (e.g., RTK receiver). This technique offers very good performances since it accounts for all reproducible phenomena, but is limited to specific applications and is quite cumbersome to implement. For other generic applications, we use an alternate empirical compensation formula that depends

on the distance and uses only 3 parameters (a, b, d_0), all expressed in meters

$$\rho_{bd}(d) = a\frac{d/d_0}{\sqrt{1+(d/d_0^2)}} + b \tag{37}$$

where a can be interpreted as the amplitude of the bias variation, b as the asymptotic bias at long ranges, and d_0 as an inflexion distance (see Fig. 13).

IV. Results

Field tests have been conducted using a multi-sensor platform developed at CEA, named *Vehloc*. As illustrated in Fig. 4, the platform comprises two stacked boards, a *processing board* based on a Raspberry PI3B for high level processing (e.g. algorithms real-time processing, data recording, connectivity etc.) and a *sensor board* based on a STM32 microcontroler for low level, time critical functions like sensors management. This board is equipped with a Ublox ZED-F9P dual-band RTK GNSS receiver, a Microelectromechanical systems (MEMS) IMU from Analog Devices with two different options (ADIS16467 or ADIS16495) offering different levels of performance (gyro bias stability of 2.5°/hour and 0.8°/hour respectively), a DW1000 UWB transceiver from Decawave with proprietary front-end that includes a low noise amplifier (LNA) with a noise figure of 0.6dB, and two odometer interfaces. The UWB transceiver is configured to achieve long ranges (e.g. channel 2, PRF=16MHz, Packet Length=1024 bits, Data Rate=110kbit/s) and the ranging protocol relies on a superframe of 100ms divided into 10 slots of 10ms, which allows a refresh rate of the full ranging sequence with 8 beacons at 10Hz. The *sensor board* also ensures accurate time synchronization between the GNSS and the UWB measurements thanks to the PPS signal delivered by the GNSS receiver.

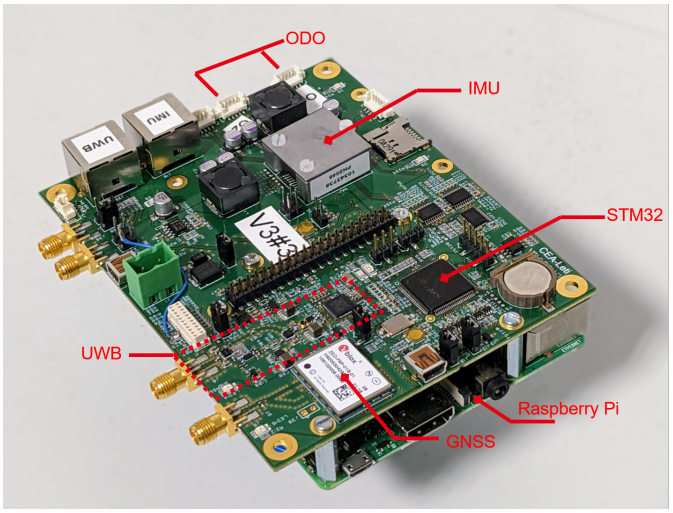

Fig. 4. Vehloc platforms for fusion.

The ground truth for position and attitude is provided by a high-end, GNSS-aided INS, such as the Ekinox or Apogee from SBG, which are post-processed using Qinertia software (from SBG) to provide centimeter-level accuracy, even in challenging GNSS conditions. The complete test setup is illustrated in Fig. 5, which shows the Vehloc platform, as well as the reference system Ekinox, mounted on a single board on the roof of a vehicle to facilitate accurate lever arm measurements. In this configuration, the GNSS antenna, the UWB radio, and the IMU are physically separated from the Vehloc platform.

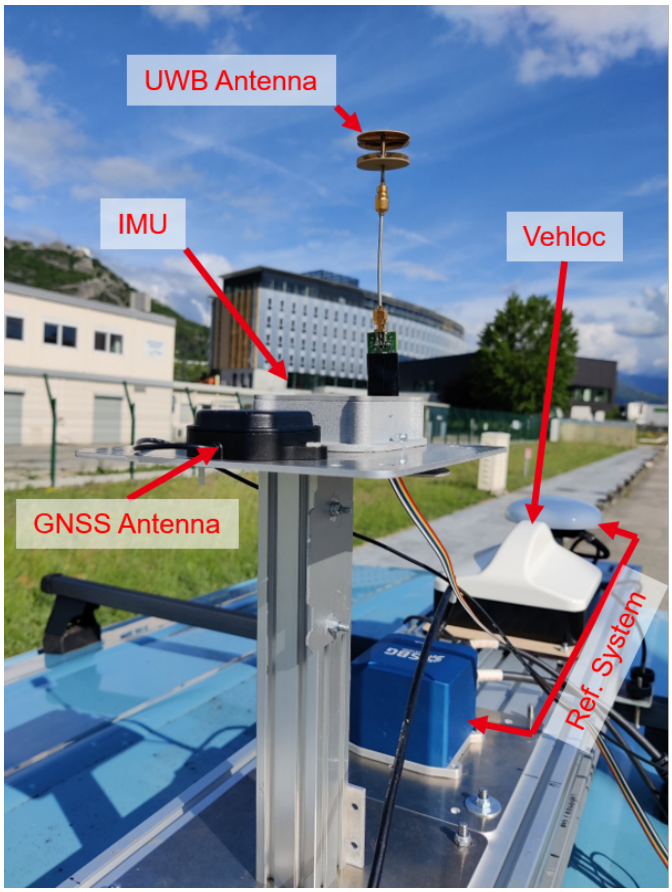

Fig. 5. Testbench for single beacon tests.

A. UWB characterisation tests

A first test campaign was conducted to calibrate UWB measurements and assess the ranging performances, especially at medium speeds (up to 50 km/h). This campaign was focused on guided applications, such as trams and trains, and only straight-line trajectories were considered. The test track used was approximately 300 meters long, with a single beacon installed on a 2-meter-high pole in the middle of the followed pathway, as shown in Fig. 6. The position of the beacon was accurately surveyed using a RTK receiver. A total of 28 tests were conducted, each consisting of one or several round trips along this track at various speeds ranging from nearly 0 km/h (i.e. small displacements of a few meters followed by short static phases) up to 50km/h. The test track was divided into 4 segments, depending on the relative position and orientation of the vehicle with respect to the fixed beacon

(see Fig. 7). The main motivation for such a split is that each segment corresponds to different propagation conditions, especially regarding the antennas radiation diagram which is modified by the presence of the vehicle. For instance, segment 1 and 3 belong to the same straight line, but on segment 1 the radio wave will experience reflections caused by e.g., the front side of the vehicle, whereas for segment 3, it is influenced by e.g., the back side of the vehicle in this specific case. Another reason justifying this split lies in the presence of an inflexion point close to the beacon antenna (see Fig. 11), which makes analytical models simpler when applied separately on each side of the antenna.

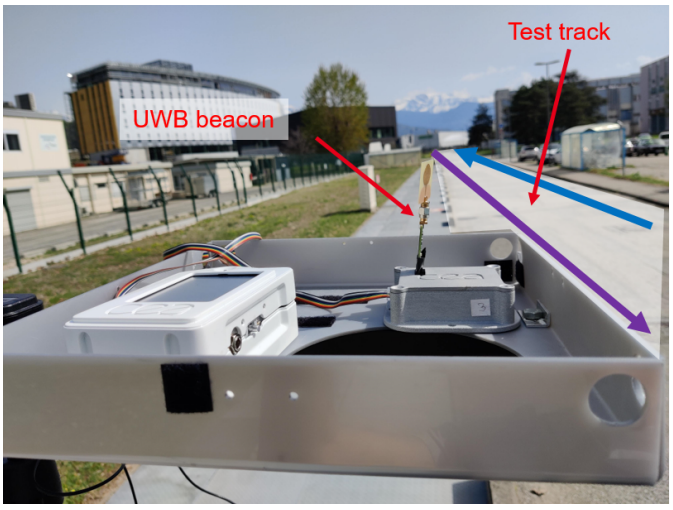

Fig. 6. Test track used for calibration tests, showing the deployed UWB beacon.

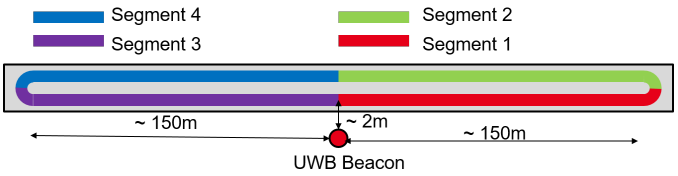

Fig. 7. Dimensions of the test track and segments definition along the followed pathway.

1) Velocity and clock compensation: Fig. 8 shows an example of measured ranges and reference distances for a test where the vehicle performed several round-trips at various speeds from 5km/h up to 50km/h (see Fig. 9) with steps of 5km/h. UWB ranges are measured at distances up to 140m with a very good coverage of all the test track. One can notice erroneous range measurements in a specific zone between 60m and 80m in segment 4 which has been later analyzed has an effect of multi-path. The computed clock drift compensation using (28) and the velocity correction using (35) are displayed in Fig. 10, and show clearly that velocity effect cannot be neglected as it introduces ranging errors of nearly 1m at 15m/s.

2) Calibration using a table: Beyond the necessary compensations of clock drift and velocity, some errors are also

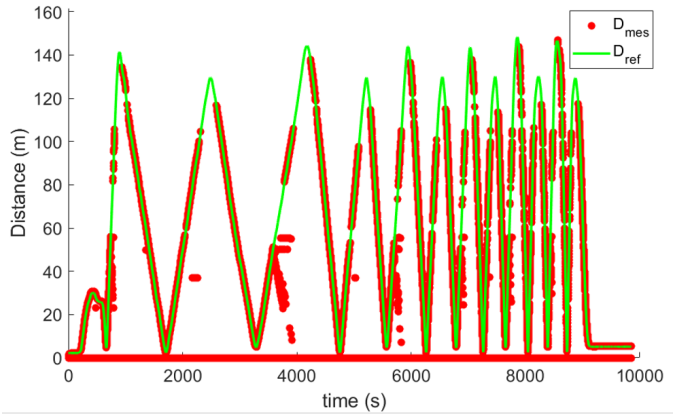

Fig. 8. Measured and reference distances.

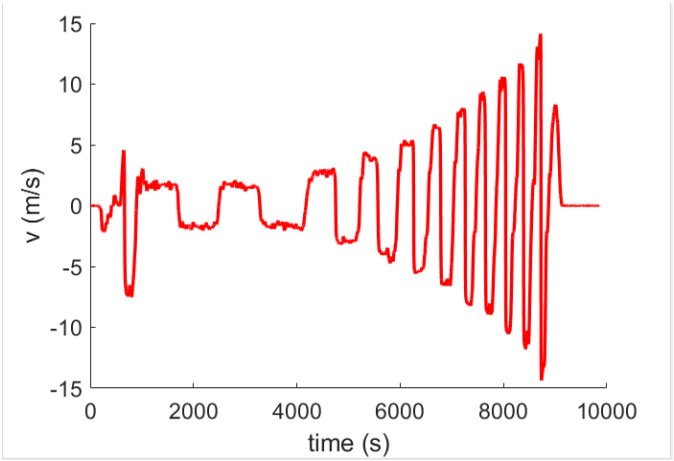

Fig. 9. Apparent velocity between the vehicle and the fixed UWB beacon.

introduced by the receiver and the propagation conditions. Fig. 11 illustrates those errors as a function of the related distances for each segment after applying velocity and clock drift compensation, as well as a coarse calibration of the measured ranges by subtracting a range bias correction of $\rho_{b0} = 154m$ [12]. Residuals errors still vary in a 80cm range, especially at short distances, mainly due to the receiver, which introduces a bias that depends on RSS and may be compensated using a calibration table [12]. However, we found in practice that this compensation does not provide very good accuracy (see table I) as the RSS measurement could be very noisy and this approach cannot take the local propagation effects into account.

When trajectories are fully reproducible, like in guided applications, one of the most efficient ways to calibrate the ranging errors is to simply measure the actual errors at every possible position of the trajectories. Although this requires preliminary on-site measurements with a reference system, it may result in the best performance as it accounts for all local propagation phenomena, which are nearly impossible to predict otherwise. A calibration table has thus been build for each segment from 0m to 100m with a 1m resolution, corresponding

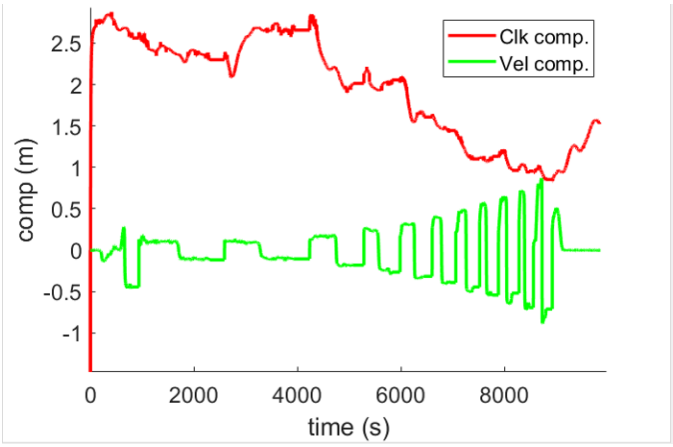

Fig. 10. Velocity and clock compensation.

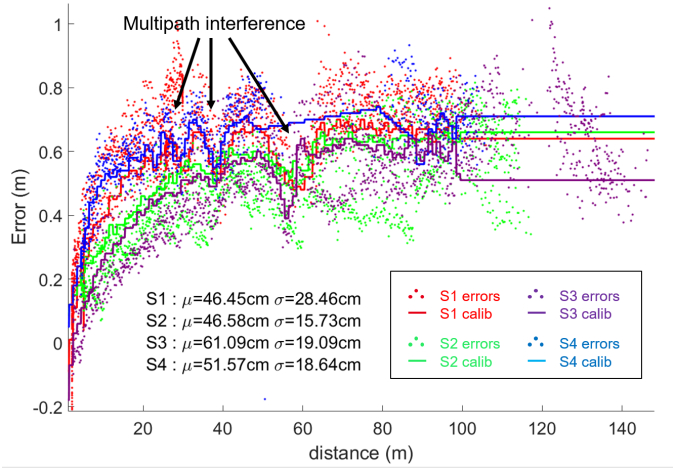

Fig. 11. UWB ranging errors vs distance before compensation from calibration table.

to 100 values per segment. A dedicated calibration experiment using very slow motion has been conducted to collect the ranging errors which are then averaged over 1m steps to construct the calibration table. Then, the calibration table has been used to correct ranging biases for other experiments. For instance, Fig. 11 shows the ranging errors and the calibration table values for the experiment corresponding to Fig. 8, which is different from the one used for calibration. One sees pretty large ranging errors that clearly depend on the distance, with a mean value of about 50cm and a standard deviation of 20cm. Although established on a different experiment, calibration values also displayed in Fig. 11 show a very good fit with measured errors, including some fast variations that have been identified as a consequence of multi-path interference. This indicates a good repeatability of these phenomena. Finally, ranging errors after compensation using the calibration table are given in Fig. 12. Flat curves indicate that the errors are essentially independent of the distance after calibration, meaning that the bias of the receiver, as well as the local propagation effects (i.e. multi-path interferences), have been

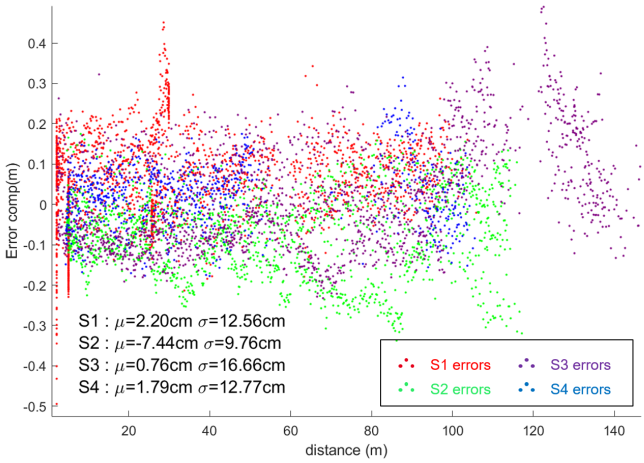

Fig. 12. UWB ranging errors vs distance after compensation from calibration table.

properly compensated. As a consequence, errors have been significantly reduced with an average bias and a standard deviation of less than 7.4cm and 16.6cm respectively in the worst case. Performances have also been measured and averaged over the 28 tests of the database (see table I), resulting in a mean bias error of less than 3cm.

3) Calibration using analytical models: As an alternative to using a calibration table, which requires a detailed survey of ranging errors, the analytical model (see (37)) can be used. This model only requires the estimation of 3 parameters. As for the calibration table in sec. IV-A2, the coefficients have been estimated separately on each segment (i.e. referred to as *Model 4*) using a dedicated calibration experiment, resulting in 12 coefficients in total. For generic applications, there is no need to distinguish between segments and only a single set of 3 parameters (referred to as *Model 1*) is necessary. Fig. 13 shows the ranging errors as well as the calibration models for the experiment described in Fig. 8. We see a good fit of the analytical models with respect to the raw errors, with only slight offsets between segments. Contrary to the approach using the calibration table, the analytical models cannot compensate the local propagation effects due to multi-path for instance.

B. Fusion test

The overall fusion scheme has been tested outdoor and, more specifically, in an 16m wide "canyon" area located in CEA premises, which is surrounded by 4-floors buildings and

TABLE I
COMPARISON OF AVERAGE RANGING ERROR BIAS OVER THE DATABASE FOR DIFFERENT CALIBRATION MODELS

Method	S1 (cm)	S2 (cm)	S3 (cm)	S4 (cm)
RSS	42,29	34,98	46,84	38,05
Calib. model1	1,03	-11,60	3,66	-11,84
Calib. model4	6,07	-3,52	2,28	8,58
Calib. table	-0,97	-2,54	-0,14	0,11

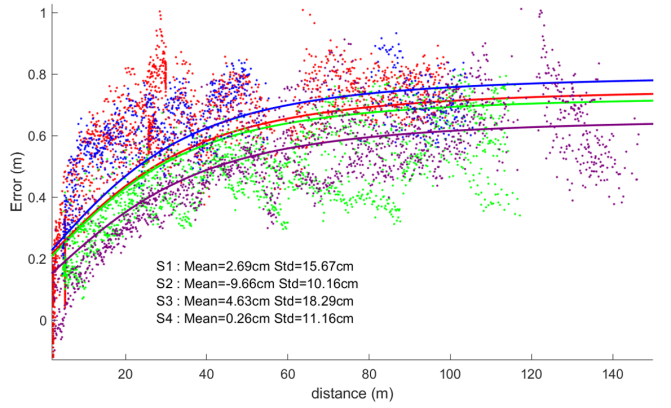

Fig. 13. UWB ranging errors and analytical calibration model.

represents a very challenging GNSS environment, as illustrated in Fig. 14. This zone is also equipped with 4 UWB beacons (numbered from 2 to 5, beacon 1 being not installed for these tests), which are permanently installed in boxes fixed to the wall at about 2.5m height, and positioned with an accuracy better than 1cm by a geometrician. The reference and the

Fig. 14. UWB beacons deployment in the canyon zone.

Vehloc platform equipped with an ADIS16467-2 IMU were both mounted on a trolley which was moved by a pedestrian describing the trajectory depicted in Fig. 15, starting with a good GNSS visibility before quickly (i.e., after less then 2mn) entering the canyon area (delimited in red in the Fig. 15) with degraded GNSS conditions but with UWB coverage. The

TABLE II
COEFFICIENTS OF THE ANALYTICAL MODELS

Segment	Model 4			Mode 1		
	a(m)	b(m)	c(m)	a(m)	b(m)	c(m)
1	0.565	0.191	41.537	0.56	0.19	40
2	0.549	0.183	39.878			
3	0.539	0.195	41.512			
4	0.529	0.130	43.460			

trajectory went into the canyon twice during the experiment (i.e. from t=349s to t=562.9s and from t=795s up to the end of the experiment) with some good GNSS conditions in between. Fig. 16 shows the GNSS positioning errors measured with

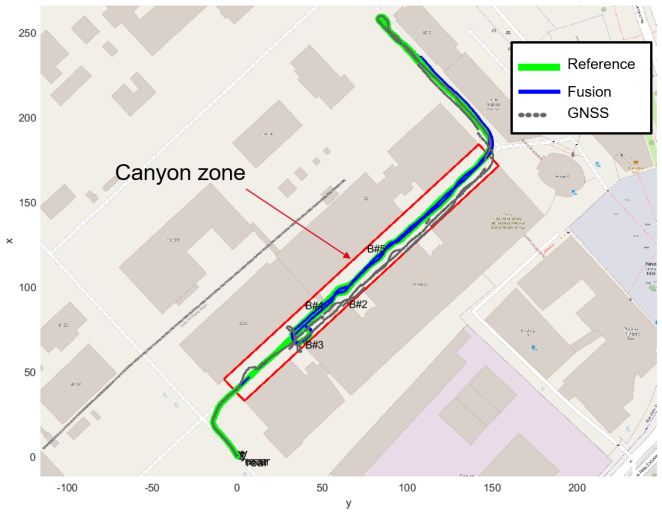

Fig. 15. Trajectory of test 1.

respect to the Apogee reference system. It also indicates the GNSS conditions (i.e. "good" when GNSS error is below 5m or "degraded" otherwise) and the RTK fix flag as background colors. In this test, the RTK fix was available out of the canyon area, providing a positioning accuracy better than 3cm. However, the two passages in the canyon correspond to a significant degradation of GNSS performances with the instantaneous loss of the RTK fix and the dramatic increase of positioning error from few cm out of the canyon, to several meters inside the canyon for the horizontal error, and even up to 25m for the vertical error. In addition, one can notice some short RTK fixes inside the canyon, which can be interpreted as an erroneous fix detection, as the corresponding positioning errors are on the magnitude order of several meters. More generally, there is a significant inconsistency in the canyon between the positioning accuracy estimated by the receiver (i.e., between 1cm for wrong RTK-fix and about 50cm at most), and the actual errors, which are 10 to 100 times larger. This inconsistency in challenging GNSS environments is one of the main limitations of the low cost RTK receivers such as the uBlox ZED-F9P compared to high-end receivers, and raises a serious problem in a fusion context because it makes very difficult the decision by the fusion engine whether to use or not the GNSS position. The measured ranges and their corresponding true distances computed from the reference system are shown in Fig. 17. The UWB coverage given in table III shows that a loose coupling UWB fusion (requiring at least 3 beacons) would have result in a very limited availability (i.e., about 6.4% of time), whereas the tight coupling fusion allows the use of UWB measurements even from a single beacon and results in a much higher availability of about 35.9%.

Fig. 18 shows the input information that is actually used by

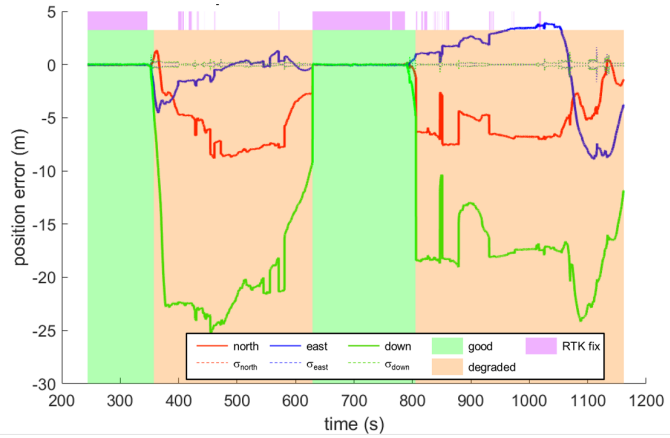

Fig. 16. GNSS errors and conditions

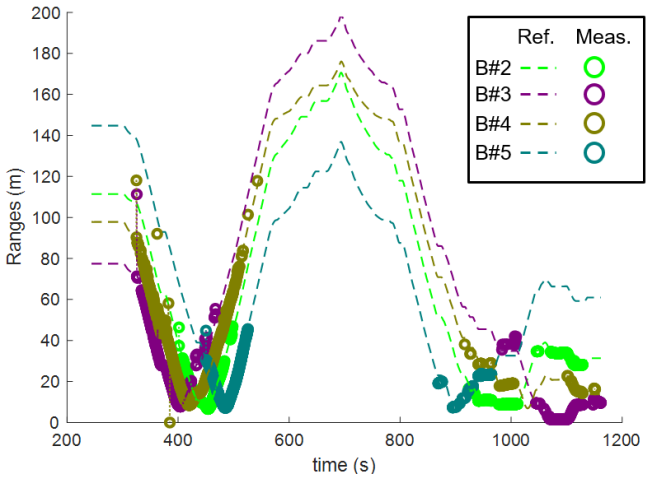

Fig. 17. UWB reference and measured ranges

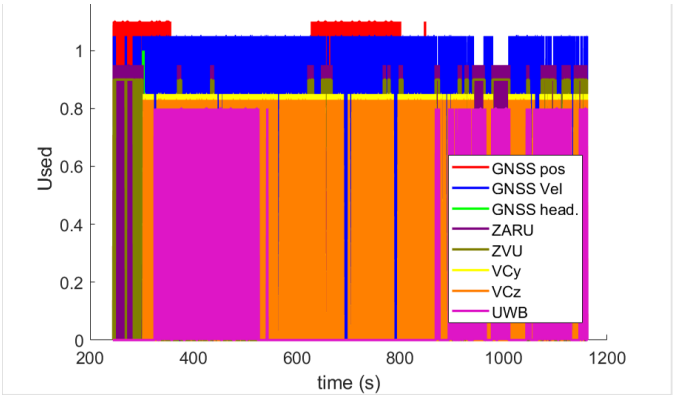

Fig. 18. Information sources that are used to correct the INS during the experiment.

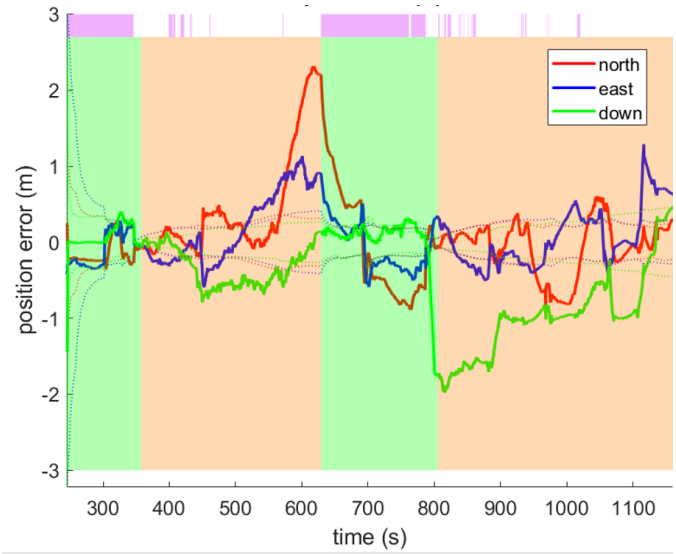

Fig. 19. Fused position error

the ES-KF for the state update according to the innovation tests (see sec. II-F), along with measurements availability. ZARU and ZVU are available at the beginning of the experiment and, in a sporadic way, during the short stops occurring in the rest of the experiment, whereas VC are used whenever the trolley is moving. Although GNSS measurements are always available, the GNSS position is discarded very quickly when entering the canyon by the innovation test, thanks to a rapid growth of the GNSS innovation, which is easily detected. GNSS velocity is more widely used as it seems more reliable even in degraded GNSS conditions. Finally, the comparison of Fig. 17 and Fig. 18 indicates that UWB is largely used when available even if about 24% of the ranging measurements are detected as outliers and rejected by the innovation test (not visible in the figure).

TABLE III
UWB AVAILABILITY FOR POSITIONING TEST.

0 beacon	1 beacon	2 beacons	3 beacons	4 beacons
64.08%	13.62%	15.88%	6.2%	0.21%

Finally the estimated position error is provided in Fig. 19 and corresponds to a P68 (i.e., 68^{th}-centile) horizontal error of 0.56m for the entire experiment and 0.40m in the canyon area, which is clearly a sub-metric accuracy. The average error outside the canyon is not at cm level because the RTK fix is not obtained immediately after exiting the canyon (i.e., the canyon is exited a t=562s and the RTK fix is obtained at t=620s), and this transition phase where UWB measurements are no more available and the GNSS error is still large also corresponds to the largest error (e.g. 2.45m at P68) due to the lack of accurate inputs. Angular errors for this experiment are 2.23deg, 0.26deg and 0.19deg for yaw, pitch and roll respectively. The same experiment has been processed without using UWB and gives almost the same performance in terms of angular accuracy but much more degraded performance for horizontal positioning with 2.1m of error in the canyon area and 1.94m for the full experiment. Beyond the refinement of the position, the UWB measurement also helps to detect and reject poor GNSS

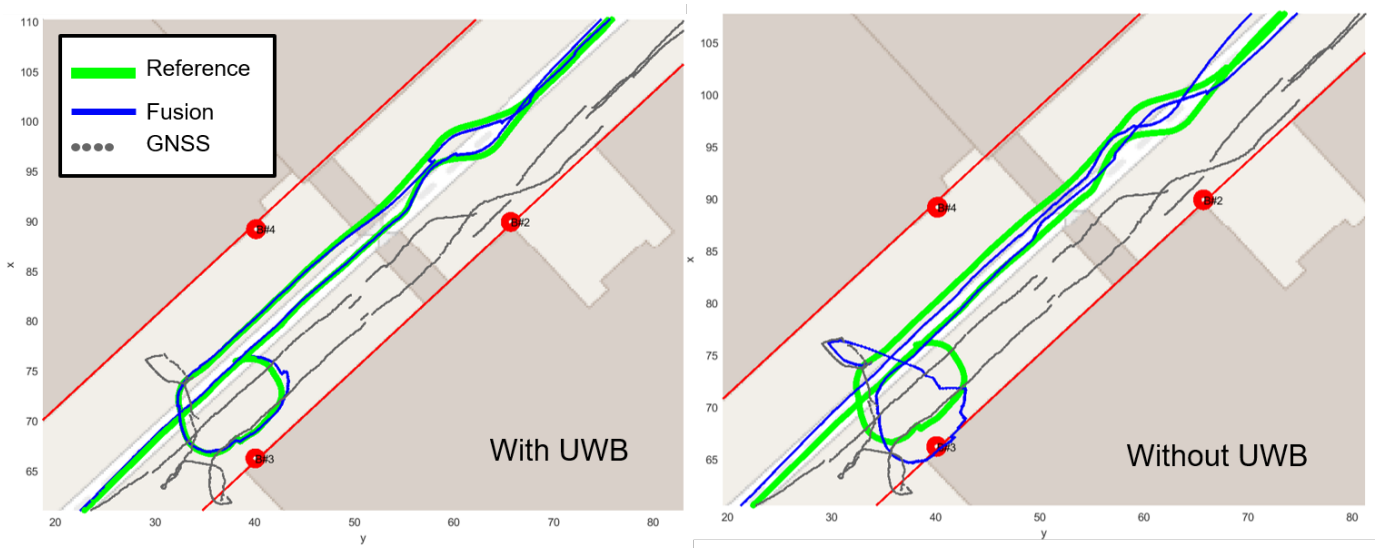

Fig. 20. Trajectories with and without UWB.

measurements. Indeed, comparing the results with and without UWB in Fig. 20 clearly shows that with the help of UWB, the GNSS positions (in gray), which are very bad in this section of the trajectory, are unused because they are rejected by the innovation test. Without UWB measurements, the covariance of the innovation (see (9)) is increasing over time due to the lack of absolute positioning information, which in turns increases the tolerance of the innovation tests and finally accepts GNSS measurements that would have been rejected otherwise, as clearly indicated in the figure by the convergence of the estimated position (in blue) toward the GNSS positions (in gray).

V. Conclusion

An UWB-aided GNSS/INS fusion algorithm using loose coupling GNSS and tight coupling UWB integration has been described. This architecture can be used to address GNSS-free areas (e.g. tunnels) equipped with full UWB network as described by other authors, but is also relevant to increase positioning performances in GNSS challenging environments (e.g. urban canyon) with limited UWB coverage, even from a single beacon. Indeed, the proposed ES-KF algorithm can dynamically adapt to available inputs and also performs signal integrity monitoring based on innovation tests to improve fusion resilience, especially in degraded GNSS conditions were the accuracy estimated by the receiver can be inconsistent with the actual positioning errors. Efficient integration of UWB measurements also requires some pre-processing for accurate synchronization with the other sensors, velocity compensation and accurate bias calibration has also been described. Regarding this latter, two approaches have been proposed, one for guided applications using a calibration table which provides ultimate performances as it also compensates for biases due to local propagation effects, and a more generic approach suitable for all use cases, which is based on a new empirical formulae. A first campaign comprising 28 tests using a vehicle equipped with a high-end reference system and a proprietary fusion platform developed at CEA has been conducted to assess UWB pre-processing performances. Beside the widely use clock drift correction, dynamic tests have also shows the effect of velocity on ranging measurements which may causes important errors of up to 1.5m at 50km/h if not properly compensated. The two calibration approaches have also been tested, resulting in a final accuracy out of the full processing of less than 3cm and 12cm over the 0m to 100m range when using the calibration table and the generic empirical formulae respectively. The fusion has been tested in a canyon area presenting degraded GNSS conditions but equipped with 4 permanently installed UWB beacons. Results have demonstrated sub-metric positioning accuracy with only 40cm of error in the canyon area despite very large GNSS errors (up to 25m), false RTK fix and inconsistent positioning accuracy delivered by the receiver. Moreover, the performances are obtained with a limited UWB coverage with full ranging measurements (i.e. by 3 or 4 beacons) only 6.4% of time and partial coverage (i.e., by 1 or 2 beacons) of 35.9%. Comparison with performances obtained without UWB ranging show a significant benefit in terms of positioning accuracy which is degraded to 2.1m in that case, but also in terms of resilience as the ranging measurements can help to detect and discard poor GNSS measurements. Finally, the developed algorithm has been integrated on the Vehloc platform using matlab generated C-code and has been tested in real-time. Ongoing work is now considering full tight fusion (i.e., GNSS and UWB) to further improve the resilience of the fusion in Challenging GNSS environments.

References

[1] Q. Zhang and X. Niu, "Research on accuracy enhancement of low-cost mems ins/gnss integration for land vehicle navigation," in *2018 IEEE/ION Position, Location and Navigation Symposium (PLANS)*, 2018, pp. 891–898.

[2] A. A. Chugunov, N. I. Petukhov, A. P. Malyshev, V. B. Pudlovskiy, O. V. Glukhov, and A. A. Frolov, "Experimental evaluation of uwb local navigation system performance used for pedestrian and vehicle positioning in outdoor urban environments," in *2021 XV International Scientific-Technical Conference on Actual Problems Of Electronic Instrument Engineering (APEIE)*, 2021, pp. 449–454.

[3] M. Malajner, P. Planinšič, and D. Gleich, "Uwb ranging accuracy," in *2015 International Conference on Systems, Signals and Image Processing (IWSSIP)*, 2015, pp. 61–64.

[4] R. Zhang, F. Shen, Y. Liang, and D. Zhao, "Using uwb aided gnss/ins integrated navigation to bridge gnss outages based on optimal anchor distribution strategy," in *2020 IEEE/ION Position, Location and Navigation Symposium (PLANS)*, 2020, pp. 1405–1411.

[5] W. Jiang, Z. Cao, B. Cai, B. Li, and J. Wang, "Indoor and outdoor seamless positioning method using uwb enhanced multi-sensor tightly-coupled integration," *IEEE Transactions on Vehicular Technology*, vol. 70, no. 10, pp. 10 633–10 645, 2021.

[6] V. Di Pietra, P. Dabove, and M. Piras, "Seamless navigation using uwb-based multisensor system," in *2020 IEEE/ION Position, Location and Navigation Symposium (PLANS)*, 2020, pp. 1079–1084.

[7] K. Cisek, K. Gryte, T. H. Bryne, and T. A. Johansen, "Aided inertial navigation of small unmanned aerial vehicles using an ultra-wideband real time localization system," in *2018 IEEE Aerospace Conference*, 2018, pp. 1–10.

[8] M. Navarro, J. Arribas, J. Vilà-Valls, J. Casademont, A. Calveras, and M. Catalán, "Hybrid gnss/ins/uwb positioning for live demonstration assisted driving," in *2019 IEEE Intelligent Transportation Systems Conference (ITSC)*, 2019, pp. 3294–3301.

[9] A. Guizar, A. Ouni, C. Goursaud, C. Chaudet, and J. Gorce, "Quantifying the impact of scheduling and mobility on ir-uwb localization in body area networks," in *2015 IEEE 12th International Conference on Wearable and Implantable Body Sensor Networks (BSN)*, 2015, pp. 1–6.

[10] P. D. Groves, *Principles of GNSS, Inertial, and Multisensor Integrated Navigation Systems, Second Edition*. Artech House, 2013.

[11] J. Zhang, W. Wang, X. She, and X. Li, "2-d indoor passive real-time location system based on ultrawideband technology," *IEEE Transactions on Instrumentation and Measurement*, vol. 71, pp. 1–17, 2022.

[12] *APS011 APPLICATION NOTE : SOURCES OF ERROR IN DW1000 BASED TWO-WAY RANGING (TWR) SCHEMES*, Decawave, 2014, rev. 1.